Cement and Concrete Research 39 (2009) 620–628

Contents lists available at ScienceDirect

Cement and Concrete Research

journal homepage: http://ees.elsevier.com/CEMCON/default.asp

Fracture mechanical behavior of concrete and the condition of its fracture surface

Viktor Mechtcherine *

Institute of Construction Materials, TU Dresden, 01062 Dresden, Germany

ARTICLE INFO

Article history:
Received 5 March 2008
Accepted 27 March 2009

Keywords:
Concrete
Heterogeneity
Fracture mechanics
Stress–crack opening relations
Fracture surfaces
Fractal geometry

ABSTRACT

In this research project, a series of uniaxial, deformation controlled tensile tests were performed in order to study the fracture mechanical behavior of concrete. The parameters under investigation were the strength of concrete, curing conditions, concrete temperature and loading rate. The fracture surfaces of the tested specimens were investigated in detail and their condition was quantified using the fractal geometry. The evaluation of the experimental results and the results of the fractological investigation displayed correlations between the shape of the stress–crack opening relation of concrete and the values of the roughness as well as the fractal dimension of its fracture surface for all parameters under investigation. Relationships were drawn between the individual material as well as test parameters and the degree of concrete heterogeneity, which proved to be decisive for the formation and propagation of cracks in concrete. It was concluded that the roughness of the fracture surfaces might be considered as a representative replica of the crack system correlating directly with the concrete heterogeneity.

© 2009 Elsevier Ltd. All rights reserved.

1. Introduction

In recent years, comprehensive research of fracture surfaces of various materials provided a deeper insight into the development of cracks. The corresponding investigations on metals were performed by Mandelbrot et al. [1]. The first measurements of crack profiles of concrete fracture surfaces were carried out by Saouma et al. [2]. Mihashi et al. [3] investigated the effect of the maximum grain size of aggregates on the fracture behavior of concrete as well as the roughness of fracture surfaces of concrete.

In this study, the effects of several further important parameters on the formation and propagation of cracks in concrete were investigated in order to better understand the decisive phenomena of concrete failure under different loading conditions.

In the first step, a series of deformation controlled uniaxial tension tests on unnotched and notched concrete prisms with non-rotatable boundaries were performed. The test parameters were the composition of concrete (normal and high strength concrete), curing conditions (sealed and unsealed), concrete temperature (2 °C, 23 °C und 50 °C) and loading rate (strain rate of 10^{-4}, 10^{-5} and 10^{-6} 1/s). The tests provided complete stress–strain and stress–crack opening relations of concrete under tension for different combinations of the parameters being investigated. The complete presentation of the results of the tension tests is given in [4]. Therefore, here, the results are only presented for the tests series, from which the fracture surfaces were taken for a subsequent fractological investigation.

In the second step, the condition of the fracture surfaces was studied on two different scales for several chosen combinations of the testing parameters. The entire fracture surfaces of the tested specimens were investigated using a relatively coarse measurement grid ("meso-scale") in order to understand fracture mechanisms and to explain the effect of the investigated parameters on the shape of the stress–crack opening diagrams (σ–w relations), which were derived from the tests on notched specimens. The components of the failure surfaces – fractured aggregate, cement paste and cement paste–aggregate interface – were investigated on a microscopic scale to provide additional information concerning the local failure mechanisms in concrete. These data were correlated to the shape of the stress–strain curves (σ–ε relations) obtained from the experiments on unnotched prisms.

2. Fracture mechanical investigations

2.1. Concrete compositions, preparation of specimens and test set-up

The composition of three types of concrete, which were investigated, is given in Table 1. Ordinary Portland cement CEM I 32.5 R was used in every mixture. Quartzite Rhine sand and gravel were used as aggregates. The mixtures HSC (high strength concrete) and NSC I (normal strength concrete) had an equal fraction of aggregates. The amount of the aggregates in concrete NSC II was higher, and its content of cement paste was correspondingly lower. The mixture for HSC had a silica fume content of 45 kg/m^3. By adjusting the dosage of a sodium naphthalene sulfonate type super plasticizer, the same nominal spread (43–47 cm) could be achieved for all three types of concrete. Their compressive strengths f_{cc}^{cube}, obtained from the tests on cube specimens at an age of 28 days, were 96 MPa, 53 MPa and 44 MPa, respectively.

* Tel.: +49 351 463 35920.
E-mail address: mechtcherine@tu-dresden.de.

0008-8846/$ – see front matter © 2009 Elsevier Ltd. All rights reserved.
doi:10.1016/j.cemconres.2009.03.011

Table 1
Composition of the concretes.

Concrete	w/c	Cement [kg/m^3]	Silica Fume [kg/m^3]	Aggregate 0–16 mm [kg/m^3]	Super plasticizer [kg/m^3]	f_{cc}^{cube} [MPa]
HSC	0.33	450	45	1721	21	96
NSC I	0.45	424	–	1721	9	53
NSC II	0.60	318	–	1811	1	44

Table 2
Selected results of the tension tests ($\vartheta = 23$ °C, $\dot{\varepsilon} = 10^{-6}$ 1/s or $\dot{\delta} = 5 \cdot 10^{-5}$ mm/s).

Concrete	f_t [MPa]	E_0 [GPa]	ε_{tu} [$\cdot 10^{-3}$]	f_{tn} [MPa]	G_F [N/m]	l_{ch} [m]
HSC, sealed	6.1 (0.2)	47.70 (0.17)	0.151 (0.005)	5.4 (0.7)	162 (21)	0.21
NSC II, sealed	3.8 (0.4)	36.32 (1.54)	0.130 (0.009)	2.9 (0.3)	135 (21)	0.34
NSC II, unsealed	3.1 (0.2)	33.06 (0.75)	0.128 (0.010)	2.7 (0.4)	167 (24)	0.57

Standard deviations are given in parentheses.

Dumbbell-shaped prisms with a gauge length of 250 mm were chosen to determine the uniaxial tensile strength f_t, the tangent modulus of elasticity E_0, as well as the σ–ε diagram for increasing stresses (see Fig. 1a). Notched prisms were used to determine fracture energy G_F and the complete stress–deformation relation. The notch depth was 20 mm. Both types of specimens had the same effective cross-section 60×100 mm^2. A schematic view of the specimen geometries and typical stress–deformation relations is given in Fig. 1b. Details may be found in [4].

All specimens were cast horizontally in metal forms. After demoulding, the specimens were wrapped in a thin plastic sheet, to which an aluminum foil was glued in order to protect the concrete against desiccation. Subsequently, the prisms were stored in a climatic room at a temperature of 23 °C and a relative humidity of 65% until shortly before testing. For the concrete NSC II, a parallel series of specimens were also kept unsealed after demoulding in a climatic chamber at the same storing conditions as the sealed specimens. All specimens were tested at an age of 56 days.

To assure stable and possible symmetrical crack propagation in the uniaxial tension tests, stiff metal plates were glued to the specimens. Finally, the metal plates were firmly attached to the bearing platens of the testing machine.

In the tests on the unnotched prisms, the strain rate was controlled by means of the average signal of two LVDTs fixed to the specimens. In the experiments on the notched specimens, four LVDTs with gauge lengths of 25 mm were placed on the notch tips on both sides of the specimen to achieve a better deformation rate control. Two further LVDTs with gauge lengths of 50 mm were placed in the middle of the notched cross-section to provide the data for the σ–δ relation, cf. Fig. 1b.

Before testing, the temperature of the specimens was adjusted to the required value in a constant environment chamber. During testing, the specimens were kept in a specially constructed climatic box within the testing machine.

The tension tests on dumbbell-shaped specimens were performed with strain rates $\dot{\varepsilon}$ of 10^{-6} 1/s, 10^{-5} 1/s and 10^{-4} 1/s, respectively. The corresponding deformation rates $\dot{\delta}$ in the tension tests on notched specimens were $5 \cdot 10^{-5}$ mm/s, $5 \cdot 10^{-4}$ mm/s and $5 \cdot 10^{-3}$ mm/s.

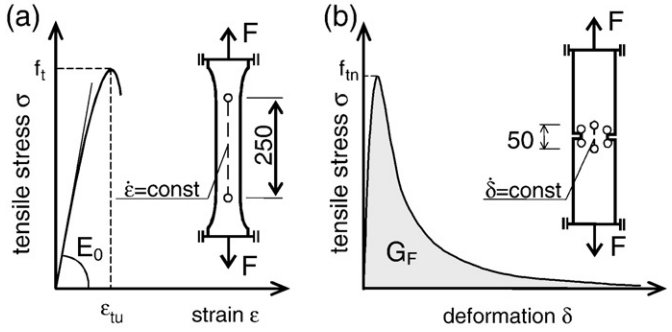

Fig. 1. Schematic view of the geometry of (a) unnotched and (b) notched specimens with schematic representation of stress–deformation relations (geometrical data in [mm]).

2.2. Main results from the fracture mechanical tests

For each chosen parameter combination, at least four specimens were tested in tension and subsequently investigated using fractological methods.

2.2.1. Effect of the concrete strength and curing conditions

From the uniaxial tension tests on unnotched prisms, characteristic stress–strain relations were obtained as shown in Fig. 1a (cf. Fig. 13 for the average measured curves). While the relation is linear at low stresses, the shape of the curve deviates from linearity at higher stresses due to the formation of micro-cracks until it becomes horizontal at $\sigma = f_t$. Stable crack propagation after peak load could not be achieved with the particular test set-up used here.

Table 2 shows that the tensile strength f_t, the tangent modulus of elasticity E_0 and the ultimate strain ε_{tu} (the strain at peak stress $\sigma = f_t$) of the HSC are significantly higher than the corresponding values for the NSC II. The unsealed normal strength concrete NSC II showed lower f_t and E_0 values and slightly lower values of the strain ε_{tu} than the sealed NSC II.

In the uniaxial tension tests on notched specimens, the descending branch of the σ–δ relation could also be determined until just before the specimens separated into two parts, due to both the localized crack developing as a result of the notches as well as reducing the gauge length for the control of deformation rate to 25 mm. The values of the net tensile strength f_{tn}, the fracture energy G_F and the characteristic length l_{ch} obtained from these experiments are listed in Table 2.

The net tensile strength f_{tn} displays a similar dependence on the concrete composition and the curing conditions compared to the tensile strength f_t measured on the dumbbell specimens; f_{tn} is however lower than f_t indicating that a notch sensitivity of the concretes exists.

The fracture energy G_F is defined as the energy per unit area needed to completely separate a specimen into two individual parts. This value corresponds to the area under the stress–crack opening relation. The crack opening w was estimated by using Eq. (1) from deformations δ measured in corresponding uniaxial tension tests on notched prisms. By doing so the elastic part of the measured deformations during both loading and unloading stage of the test was excluded.

$$w = \delta - \sigma \cdot \delta_{tu,n} / f_{tn} \tag{1}$$

with

σ tensile stress
$\delta_{tu,n}$ deformation at reaching tensile strength f_{tn}.

The fracture energy of the high strength concrete HSC is higher than the corresponding value of the sealed normal strength concrete NSC II, but slightly lower than the fracture energy of the unsealed NSC II.

The characteristic length l_{ch} was calculated according to the following formula by Petersson [13]: $l_{ch} = G_F \cdot E_0 / f_t^2$. It gives the half-length of an imaginary tensile specimen, in which the release of the

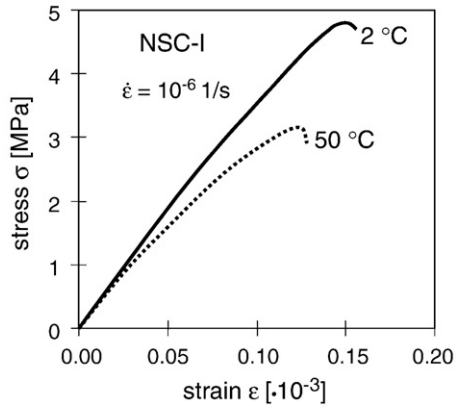

Fig. 2. Effect of the temperature on the stress–strain relation, average curves.

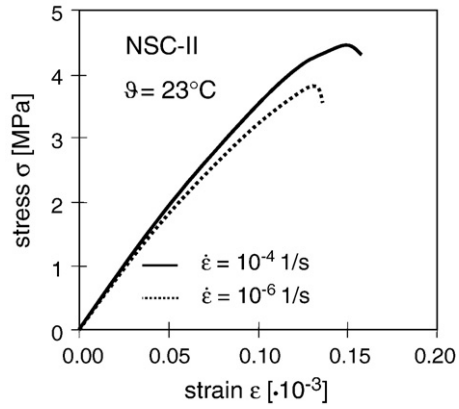

Fig. 3. Effect of the strain rate on the stress–strain relation, average curves.

potential deformation energy after cracking is equal to the energy dissipation due the crack formation and complete crack opening, i.e. to a complete separation of the specimen into two parts. The characteristic length l_{ch} decreases with an increase in concrete strength. The specimens composed of the NSC II and protected from desiccation displayed a smaller characteristic length than those of the unsealed concrete. The higher l_{ch} values indicate a less brittle concrete behavior.

2.2.2. Effect of the temperature and loading rate

The average stress–strain curves obtained from the tension tests on unnotched prisms at different temperatures and strain rates are shown in Figs. 2 and 3. The results of the evaluation of these curves as well as from the tests on notched specimens are given in Table 3. The tensile strength f_t, modulus of elasticity E_0 and ultimate strain ε_{tu} decrease with increasing temperature ϑ. An increase of the strain rate $\dot{\varepsilon}$ results in an increase of these material parameters.

According to Table 3, no clear effect of the temperature ϑ or deformation rate $\dot{\delta}$ on the fracture energy G_F was observed. The characteristic length l_{ch} decreases with decreasing temperature and increasing loading rate, which indicates a more brittle fracture at these testing conditions.

3. Fractological investigations

3.1. Measuring technique

3.1.1. Projected fringes technique

To study the investigated parameter effects on the crack propagation, fracture surfaces from the uniaxial tension tests were first measured using the projected fringes technique (Fig. 4). Height differences of the surface induce a lateral displacement of the projected strip pattern. The incorporation of geometrical data of the optical configuration then allows the contour information to be detected from the phase shift of the surface strip pattern at each surface location [5,6]. The measurement at intervals of 0.16 mm provided 375×625 mesh data for each entire fracture surface.

3.1.2. Confocal microscope technique

The confocal microscope technique was applied in order to investigate the condition of the components of fracture surfaces. In the confocal microscope, laser light reflected from a dichroic mirror into a scanning device moves in a raster scan in an x–y plane (Fig. 5). A point source is imaged in the object plane. The light reflected by the object is directed to a photo-multiplier via a small aperture, which excludes light coming from above or below the focal plane ensuring that only information from the focal plane reaches the detector. By coupling a step motor to the focusing unit whole series of sectional images can be produced by changing the focal plane. This information is used to rebuild a three dimensional image of an object by overlaying the images of a section series [7].

In this study, 512×512 mesh data have been used for each monitored spot of 0.64 mm×0.64 mm.

3.2. Quantification of the condition of fracture surfaces

From the optical measurement data, the roughness $R_{S,l_{min}}$ and the fractal dimension D of the surfaces were determined in order to quantify the condition of the entire fracture surfaces as well as of their components.

3.2.1. Grid Scaling method

The roughness R_S of the fractured surface was defined as a quotient of an optically measured surface area A_l and the projected area A_0. The roughness $R_{S,l_{min}}$ (Eq. (2)) was determined by applying the finest grid size l_{min} as obtained from optical measurements. This means that geometrical data of all measured points were used to build a triangle grid (grey surface in Fig. 6a), from which the area of individual triangles and eventually of the entire surface (= the sum area of all individual triangles) was calculated.

$$R_{S,l_{min}} = \frac{A_{l_{min}}}{A_0}. \quad (2)$$

The Grid Scaling method is based on the fact that the measured surface area A_l, and herewith the roughness R_S, increase as the grid

Table 3
Selected results of the tension tests — effects of the temperature and the strain rate.

Concrete	ϑ [°C]	$\dot{\varepsilon}$ [1/s]	f_t [MPa]	E_0 [GPa]	ε_{tu} [$\cdot 10^{-3}$]	f_{tn} [MPa]	G_F [N/m]	l_{ch} [m]
NSC I,	2 °C	10^{-6}	4.8 (0.3)	38.56 (0.63)	0.150 (0.006)	4.0 (0.3)	132 (19)	0.22
sealed	50 °C	10^{-4}	3.2 (0.2)	34.77 (0.30)	0.123 (0.008)	3.0 (0.4)	127 (15)	0.44
NSC II,	23 °C	10^{-6}	4.5 (0.1)	38.71 (0.97)	0.150 (0.006)	3.8 (0.4)	145 (14)	0.28
sealed			3.8 (0.4)	36.32 (1.54)	0.130 (0.009)	2.9 (0.3)	141 (21)	0.35

Standard deviations are given in parentheses.

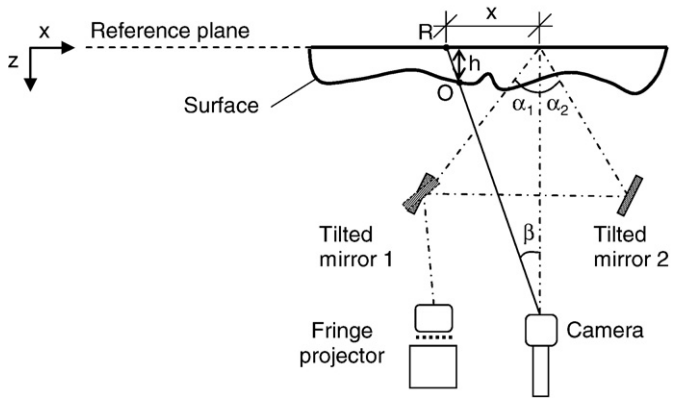

Fig. 4. Principle of the projected fringes technique according to [6].

size l decreases. This relationship is governed by the fractal increment d_{GS} as shown in Eq. (3).

$$R_S = R_{S,l_{min}} \cdot l^{-d_{GS}} \tag{3}$$

with

R_S	roughness of the fracture surface for grid size $l = \eta \cdot l_{min}$
d_{GS}	fractal increment of the fracture surface
η	scaling factor.

Coarser grids were produced by neglecting a corresponding number of measurement points between each two neighboring points considered in the calculation (e.g. for a grid size $l = 4 \cdot l_{min}$, only every fourth measured point was considered, cf. Fig. 6b).

In order to calculate the Grid Scaling fractal dimension, the logarithm (ln) of the roughness R_S must be plotted against the logarithm (ln) of the grid size. The slope of the regression line gives the value of fractal increment d_{GS} (Fig. 7). The Grid Scaling fractal dimension D_{GS} can be calculated by adding this value to the dimension of a plane = 2. A similar evaluation procedure was successfully applied by Mihashi et al. [3] and Carpinteri et al. [12].

The accuracy of the Grid Scaling method was successfully tested by calculating the Grid Scaling fractal dimension for a number of self-similar fractal sets (e.g. Koch surfaces, whose fractal dimension (Hausdorff–Besicovitch Dimension) is known to be 2.2619) and comparing the obtained result with the expected one.

3.2.2. Cube Counting method

This method is an extension of the Box Counting method, successfully applied for studying fracture profiles by Saouma et al. [2]. However, instead of squares, cubes of different sizes are generated over the 3D contour data (Fig. 8). The number of cubes N intersecting the surface, divided by the number of cubes s^2 necessary to cover the projection surface, is plotted with respect to the inverse of the cube size l on a ln–ln scale. If a linear relationship is found, then the Cube Counting fractal dimension D_{CC} can be determined by adding the fractal increment d_{CC} (which corresponds to the slope of the linear regression line) to the dimension of a plane = 2 (Fig. 9).

3.3. Results of the fractological investigation

3.3.1. Effect of the concrete strength and curing conditions

Typical contours of a fracture surface of the sealed high strength concrete (HSC) and the unsealed normal strength concrete (NSC II) obtained from the optical measurements using the Projected Fringes technique are shown in Fig. 10. They are in essence identical with photographic images of the corresponding fracture surfaces, however the computed contours provide a clearer graphical presentation. The

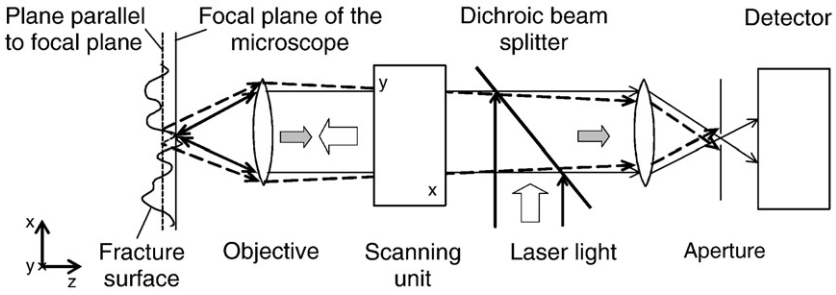

Fig. 5. Basic concept of a confocal laser scanning microscope.

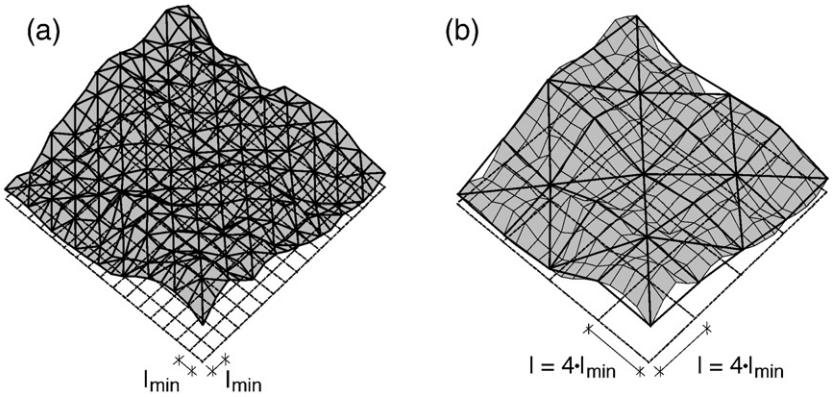

Fig. 6. Schematic view of Grid Scaling method — coverage of the fracture surfaces by networks of triangles using a grid size (a) l_{min} and (b) $l = 4 \cdot l_{min}$, respectively.

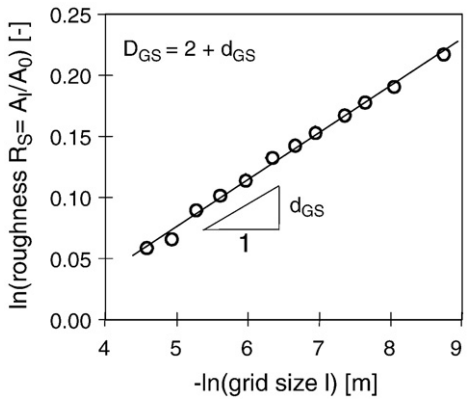

Fig. 7. Plot of Grid Scaling method applied to the fracture surface of a concrete specimen (here: NSC II, sealed).

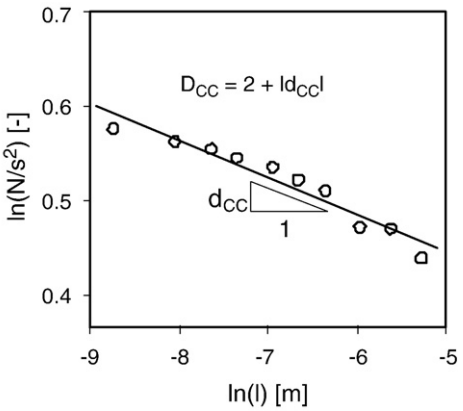

Fig. 9. Plot of Cube Counting method applied to the fracture surface of a concrete specimen (here: NSC II, sealed).

failure of the coarse aggregates is evident in the case of HSC, while the cracks in NSC II developed in the contact zone between the aggregates and the cement paste, which resulted in no aggregate failure.

Table 4 gives the results of the fractological measurements and calculations for the entire fracture surfaces. The roughness $R_{S,l_{min}}$ was obtained for the grid size of 0.16 mm. The roughness and both fractal dimensions D_{GS} and D_{CC} increase with decreasing strength of concrete. The fracture surfaces of the unsealed normal strength concrete are rougher than those of the sealed NSC.

The values of the Cube Counting dimension were generally found to be slightly higher than the values of the Grid Scaling dimension.

Table 5 gives the results based on the investigation of the components of fracture surfaces using a confocal microscope. The differentiation of cement paste, broken aggregates and cement paste–aggregate interface, and subsequently the choice of the spots to be investigated, were performed by visual control prior to the use of the confocal microscope.

The roughness $R_{S,l_{min}}$ was derived from the surface area measured with a grid size of 1.252 μm. According to Table 5, the micro-roughness and fractal dimensions D_{GS} and D_{CC} of the fractured cement paste of HSC are lower than the corresponding values of NSC II. The fractured cement paste of the unsealed NSC II has the roughest surface. The cement paste–aggregate interface of the unsealed NSC II is also rougher than that of the sealed NSC II. The fractured aggregates of the high strength concrete provided a rather strong variation of the R_S and D_{GS} values. This was caused by a significant dissimilarity of the microstructure of the aggregate grains investigated.

3.3.2. Effect of the temperature and loading rate

The investigation results on the effect of the temperature and loading rate on the condition of the entire fracture surfaces of concrete specimens are given in Table 6. With increasing temperature, a slight but clear increase of the roughness $R_{S,l_{min}}$ and the fractal dimensions D_{GS} and D_{CC} could be observed. The increase of the deformation rate resulted in smoother fracture surfaces.

4. Discussion of the results

4.1. Effect of the concrete strength and curing conditions

With increasing concrete strength, an increase of the ultimate strain ε_{tu} was observed (Table 2 and Fig. 11). Drying of the normal strength concrete had no significant effect on this material parameter. However, considering only the non-linear deformation component of the strain $\varepsilon_{tu,nl}$ ($\varepsilon_{tu,nl} = \varepsilon_{tu} - f_t / E_0$), the highest values are obtained for the unsealed NSC II and the lowest ones for HSC. The σ–ε relation of NSC II is more non-linear than that of the HSC probably due to the advanced micro-cracking in the case of NSC II. Fig. 12 shows calculated non-linear strains ε_{nl} ($\varepsilon_{nl} = \varepsilon - \sigma / E_0$), i.e. strains caused by micro-cracking. The unsealed NSC II provided the most pronounced non-linearity.

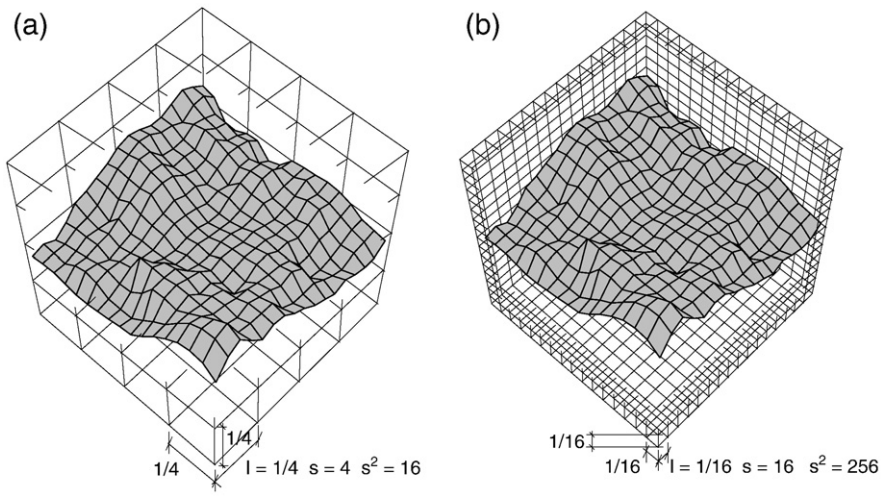

Fig. 8. Schematic view of Cube Counting method — coverage of the fracture surfaces by 3-dimensional lattices (here for two different cube sizes: (a) $l = 1/4$ and (b) $l = 1/16$).

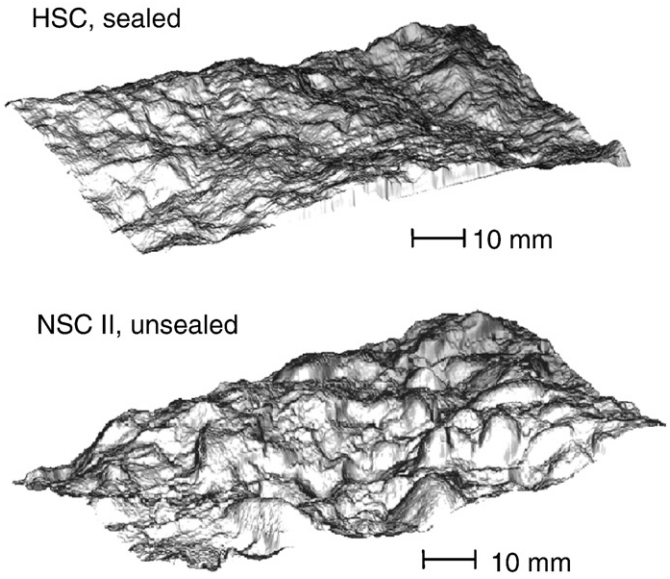

Fig. 10. Typical contours of fracture concrete surfaces.

The non-linear strains, which represent a measure of the damage in concrete due to micro-cracking, correlate to the values of the roughness $R_{S,l_{min}}$ and the fractal dimensions D_{GS} and D_{CC} detected for the components of the fracture concrete surfaces on the micro-level (cf. Table 5). The reason for this correlation is not self-evident, since there is no exact knowledge concerning the spatial distribution and interaction of micro-cracks. However, there are some indications, which might explain this phenomenon. The measurements using the Acoustic Emission technique performed by Kessler-Kramer et al. [8] clearly show that before the tensile strength is reached, a considerably larger number of acoustic events occur during loading of high strength concrete in comparison to normal strength concrete. On the other hand, the corresponding non-linear deformations of high strength concrete are smaller. Combining both of these facts, we must assume that a larger number of finer cracks form in HSC, when once again comparing it to NSC. We can therefore conclude that individual micro-cracks in HSC should be positioned closer to each other in any direction. It should therefore be possible for a crack to form by connecting close-by cracks, which will produce smoother crack paths and a correspondently smoother fracture surface in the case of HSC. This agrees with the results of the performed measurements of the surface roughness. It can therefore be concluded that the smaller number of larger micro-cracks in normal strength concrete, especially in the unsealed case, must cause a rougher fracture surface.

The reason for the formation of coarser micro-cracks in the cement paste of NSC II in comparison to HSC might be an increase in capillary porosity with increasing w/c ratio. A relatively coarse pore system, which can be associated with a high water content of the mixture, is likely the main cause for more uneven crack paths and, as a result, a rougher fracture surface in the case of a concrete possessing a higher w/c ratio (here NSC II). For the unsealed NSC II specimens this effect seems to be even more pronounced, since the hydration of cement and the formation of C–S–H gel structure are decelerated due to loss of capillary water.

The uniaxial tension tests on the high strength concrete provided approximately 20% higher values of the fracture energy than the corresponding values of the sealed normal strength concrete. However, for the unsealed NSC II, a slightly higher G_F value was found in comparison to HSC.

Fig. 13 displays the influence of the concrete strength and the curing conditions on the shape of the stress–crack opening relation. (Note that the crack opening w was estimated by using Eq. (1) from deformations δ measured in corresponding uniaxial tension tests, i.e. the elastic part of the measured deformations was excluded. This holds true for all following stress–crack opening or energy dissipations–crack opening curves in this paper.) For HSC, the area under the initial part of the σ–w relation is larger than that of NSC II, because of a higher tensile strength. This indicates an increase of energy dissipation due to the formation and propagation of narrow cracks with increasing strength of concrete (cf. Fig. 14). For larger crack widths, this trend reverses and the σ–w relations for NSC II are above those of HSC. This difference is small in the case of the sealed NSC II, but it is significant in the case of the unsealed NSC II. The condition of the fracture surfaces delivers an explanation for this phenomenon: the higher roughness and the higher fractal dimensions of the fracture surfaces of NSC II, especially of the unsealed ones (see Table 4), suggest a more pronounced crack surface interlocking, which provides a better transfer of the tensile stresses across the crack. Numerical analysis by Mechtcherine and Müller [9] illustrated how this mechanism works.

It must be admitted here that the crack surface interlocking is only one of the working mechanisms. Other phenomena such as crack face bridging and crack branching play an important role concerning the transfer of tensile stresses and the energy dissipation as well. As it will be argued in Section 4.4, all these phenomena depend on concrete heterogeneity, and in this sense they are all interconnected.

4.2. Effect of the temperature

Fig. 15 shows the influence of temperature on the shape of the stress–crack opening relation. The area under the initial part of the σ–w

Table 4
Roughness and fractal dimensions of concrete fracture surfaces of the investigated concretes.

Concrete	Roughness $R_{S,l_{min}}$ [−]	Fractal dimension D_{GS} [−]	Fractal dimension D_{CC} [−]
HSC, sealed	1.167 (0.008)	2.029 (0.001)	2.032 (0.002)
NSC II, sealed	1.258 (0.013)	2.044 (0.003)	2.047 (0.004)
NSC II, unsealed	1.323 (0.040)	2.052 (0.003)	2.060 (0.006)

Standard deviations are given in parentheses.

Table 5
Roughness and fractal dimension of the fracture surfaces of the concrete components.

Concrete	Components	Roughness $R_{S,l_{min}}$ [−]	Fractal dimension D_{GS} [−]	Fractal dimension D_{CC} [−]
HSC, sealed	Cement paste	1.636 (0.239)	2.087 (0.027)	2.093 (0.030)
	Fract. aggregate	1.238–2.368	2.047–2.184	2.052–2.195
NSC II, sealed	Cement paste	1.718 (0.047)	2.097 (0.016)	2.101 (0.019)
	CP/agg. interface	1.465 (0.137)	2.080 (0.019)	2.087 (0.020)
NSC II, unsealed	Cement paste	1.940 (0.159)	2.119 (0.011)	2.122 (0.018)
	CP/agg. interface	1.782 (0.147)	2.111 (0.011)	2.113 (0.023)

Standard deviations are given in parentheses.

Table 6
Effect of the temperature and deformation rate on the roughness and fractal dimension of concrete fracture surfaces.

Concrete	Temperature [°C]	$\dot{\delta}$ [mm/s]	Roughness $R_{S,l_{min}}$ [−]	Fractal dimension D_{GS} [−]	Fractal dimension D_{CC} [−]
NSC I	2	$5\cdot10^{-5}$	1.232 (0.010)	2.040 (0.001)	2.043 (0.002)
	50		1.266 (0.005)	2.043 (0.001)	2.045 (0.002)
NSC II	23	$5\cdot10^{-3}$	1.241 (0.011)	2.039 (0.001)	2.043 (0.006)
		$5\cdot10^{-5}$	1.259 (0.009)	2.043 (0.001)	2.046 (0.001)

Standard deviations are given in parentheses.

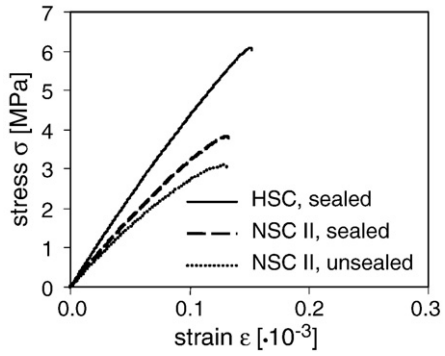

Fig. 11. Measured σ–ε relations for the normal strength (NSC II) and the high strength (HSC) concretes, average curves.

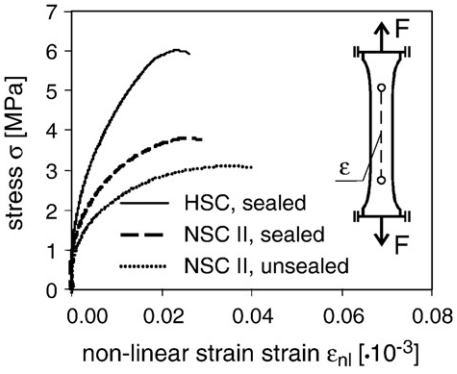

Fig. 12. Calculated non-linear strains ε_{nl} at different stress levels for the normal strength (NSC II) and the high strength (HSC) concretes, average curves.

curve increases at lower temperatures, which indicates an increase of energy dissipation for the formation and propagation of narrow cracks with decreasing temperature (cf. Fig. 16). For larger crack widths, this trend reverses, and the σ–w relations measured at higher temperature are above those measured at the lower temperature. As a result, fracture energy does not change significantly with a change of temperature in the investigated temperature range.

The higher roughness and the higher fractal dimensions of the fracture surfaces of the specimens tested at 50 °C (Table 6), and consequently a better transmission of tensile stresses over cracks, give an explanation for this phenomenon. Rougher fracture surfaces result from a more pronounced variation of properties of the material structure at higher temperatures (see also Section 4.4).

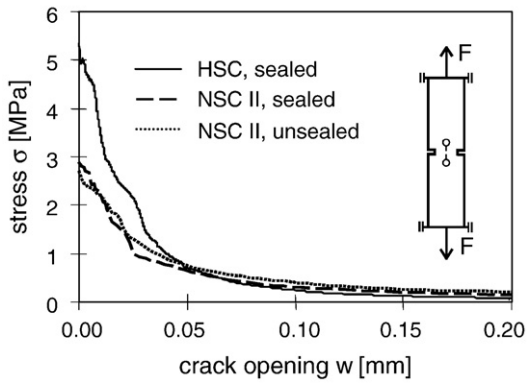

Fig. 13. Influence of the concrete strength and curing conditions on the shape of the σ–w relation, average curves.

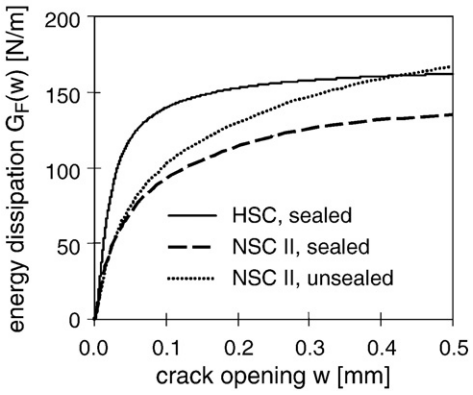

Fig. 14. Influence of the concrete strength and curing conditions on the energy dissipation due to the fracture process, average curves.

4.3. Effect of the loading rate

The σ–w relation for the high strain rate is above that for the lower strain rate for small values of w as shown in Fig. 17, whereas this trend is reversed for large crack openings (see also Fig. 18 for the energy dissipation). The data given in Table 6 also show a slight, however significant, increase in roughness and fractal dimension at the fracture surfaces with decreasing deformation rate.

4.4. Generalized evaluation of the results

Summarizing the observed tendencies and correlations, it can be concluded that the roughness of the fracture surfaces increases, both on the microscopic and mesoscopic observation levels, with a decreasing brittleness of concrete and with an increasing degree of its heterogeneity. A result of a more brittle fracture is fracture surfaces with a higher portion of broken aggregates.

Certainly, a fracture surface literally represents only one major crack in concrete, and it might be argued that such important phenomena as crack face bridging and crack branching cannot be considered in this kind of analysis. However, a numerical analysis of cracking in concrete with different degrees of heterogeneity performed by Mechtcherine and Müller [10] illustrated that both these mechanisms become more pronounced with increasing concrete heterogeneity. The numerical simulation also demonstrated that the process zone became wider with increasing heterogeneity. The roughness of individual crack paths increased as well. It was further shown that the roughness of the fracture surfaces typically correlates to the area under the second, shallow part of σ–w relations. At this stage of crack

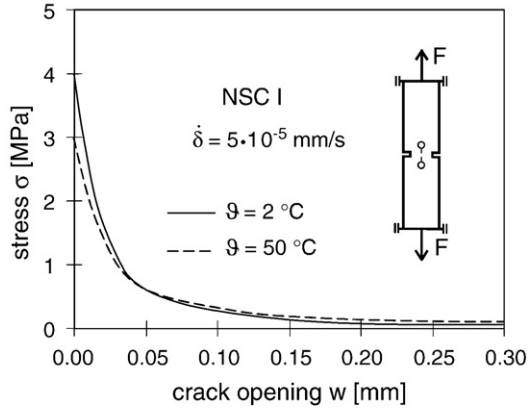

Fig. 15. Temperature effect on the shape of the σ–w relation, average curves.

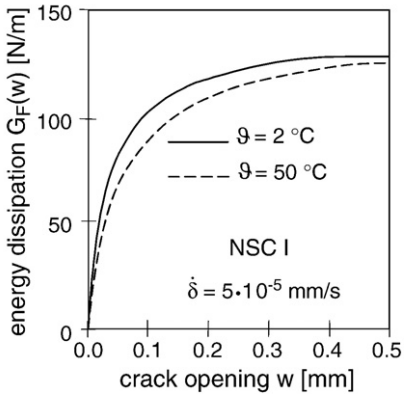

Fig. 16. Temperature effect on the energy dissipation for the crack opening, average curves.

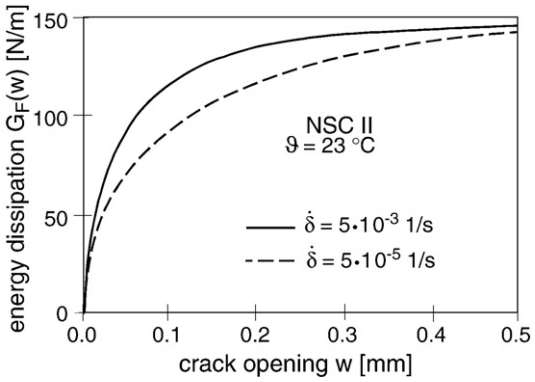

Fig. 18. Effect of the deformation rate on the energy dissipation for the crack opening, average curves.

development, the crack surface interlocking of rougher cracks becomes most pronounced.

From the considerations indicated above, it can be concluded that the condition of the fracture surface, i.e. of the final crack, is a natural product of the development of a crack system and is therefore characteristic not only for the last moment of rupture. Rougher fracture surfaces go along with a more pronounced crack branching and crack bridging, and consequently to a wider process zone [4]. This means that a fracture surface can be considered as a low-dimensional, but representative replica of the entire crack system in concrete. The found correlations between the degree of the concrete heterogeneity and the roughness of fracture surfaces confirm this assumption.

There are numerous mechanisms, which may influence the heterogeneity of concrete and consequently its brittleness. For high strength concrete, it was shown that the cement paste and the bond between aggregates and cement paste are much stronger than in the case of normal strength concrete; their mechanical properties are comparable with those of aggregates. Consequently, in high strength concrete subjected to high loading, the cracks run directly through aggregates instead of attempting to follow "falsely" oriented, dense routes around the aggregates. As a result, high strength concrete, being a more homogeneous material, displays a more brittle failure in comparison to normal strength concrete.

The desiccation of concrete at an early age causes the shrinkage of cement paste, while aggregates remain unaffected. The stress concentrations due to restraint deformations result in the formation of micro-cracks in the bond zone, first of all at larger aggregates even before any external mechanical loading occurs [11]. Due to the weakening of the bond, the crack follows the route of the lowest local resistance alongside the bond. This route is longer and it tends to start branching, which results in a higher overall energy dissipation for the crack development. Consequently, for the unsealed and due to micro-cracks induced by shrinkage, more heterogeneous concrete, a less brittle behavior as well as rougher fracture surfaces could be observed in the experiments in comparison to the sealed concrete.

With increasing temperature, the strength of cement paste decreases more pronouncedly than the strength of mortar [14], so that it is likely that the effect of the temperature changes on the strength of normal weight aggregates is less pronounced than on the strength of cement paste. This means that with increasing temperature, the degree of concrete heterogeneity increases as well. The probability of the crack propagation alongside the bond becomes higher compared to a lower temperature. The result is a less brittle failure in combination with a rougher fracture surface.

There are certainly further parameters, which influence the brittleness of concrete besides the degree of heterogeneity. In this study, it was the loading rate. A probable explanation is as follows. The crack propagation in concrete is a time dependent process. In the case of a rapid loading, the energy supply per time unit is considerably higher than would be required for the crack growth in the case of a slow loading. Due to this oversupply of energy, the crack must not take the energetically easiest route, but "chooses" a straighter route, which often leads through the aggregates (see e.g. also [15,16]. A smoother fracture surface and a more brittle fracture observed in the experiments confirm this consideration.

Summarizing the obtained results, it can be stated that a more brittle fracture always manifests itself in smoother fracture surfaces. In this context, the characteristic length l_{ch} was confirmed to be an appropriate material parameter to indicate the brittleness of concrete. Fig. 19 displays a clear correlation between the characteristic length l_{ch} of concrete for various parameters under investigations and the roughness

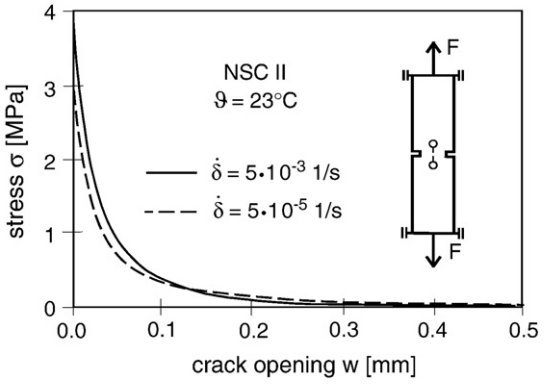

Fig. 17. Effect of the deformation rate on the shape of the σ–w relation, average curves.

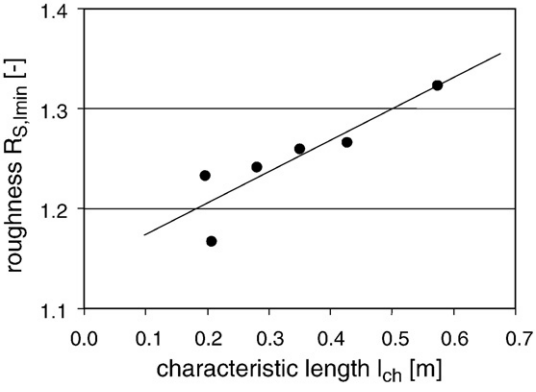

Fig. 19. Correlation between the characteristic length l_{ch} of concrete for various parameters under investigation and the roughness $R_{S,l_{min}}$ of fracture surfaces.

$R_{S,l_{min}}$ of the fractured surfaces as obtained from the fractological investigation.

5. Summary

In this research project, the effect of the strength and temperature of concrete, curing conditions as well as loading rate on fracture mechanical behavior of concrete was investigated. For a better understanding of the decisive mechanisms of concrete failure, fracture surfaces obtained from the fracture mechanical experiments were studied in detail using different measurement and evaluation techniques. The evaluation of the experimental results and the results of the fractological investigation provided correlations between the shapes of the stress–strain or stress–crack opening relations and the values of the roughness and the fractal dimension of the fracture surfaces for all test parameters under investigation. Summarizing the results, the following conclusions can be drawn:

- With increasing temperature and decreasing concrete strength as well as due to concrete desiccation at an early age, the heterogeneity of concrete increases, first of all due to a weakening of the cement matrix or/and the bond between cement matrix and aggregates. A higher degree of the concrete heterogeneity results in a more developed crack system, i.e. a more pronounced crack branching and bridging and subsequently rougher crack profiles. Consequently, higher values of the roughness and the fractal dimension of fracture surfaces are obtained for a concrete with a higher heterogeneity.
- The non-linearity of the σ–ε relation, which represents a measure of the damage in concrete due to micro-cracking, correlates with the values of the roughness and the fractal dimension detected for the components of the fracture surfaces of concrete on the microscopic level of observation.
- The higher roughness and the higher fractal dimension of the entire fracture surfaces of the investigated concretes for particular combinations of testing parameters indicate a better transfer of tensile stress across the crack. Along with the crack bridging and crack branching, this can be traced back to a more pronounced interlocking of rougher crack surfaces. These phenomena result in a less steep shape of the σ–w relation and in a higher energy dissipation at larger crack widths, though a less brittle failure of concrete.
- With an increasing loading rate, the failure of concrete becomes more brittle resulting in a steeper shape of the stress–crack opening curve. This can be traced back to an oversupply of energy at rapid loading, which enables the crack to take a straighter route, which often leads through the aggregates. As a result, smoother fracture surfaces can be observed in the experiments with higher loading rates.
- The characteristic length l_{ch}, which indicates the brittleness of materials, correlates with the roughness of the fracture surfaces of the tested concretes for different parameters under investigation.

References

[1] B.B. Mandelbrot, D.E. Passoja, A. Paullay, Fractal character of fracture surfaces of metals, Nature 308 (1984) 721–722.
[2] V.E. Saouma, C.C. Barton, N.A. Gamaleldin, Fractal characterisation of fracture surfaces in concrete, Engineering Fracture Mechanics 35 (1990) 47–53.
[3] H. Mihashi, N. Nomura, T. Umeoka, Fracture mechanics parameters of cementitious composite materials and fractured surface properties, Europe–U.S. Workshop on Fracture and Damage in Quasibrittle Structures, Prague, 1994.
[4] V. Mechtcherine, Investigations on Crack Spreading in Concrete, Doctoral thesis, University of Karlsruhe, in German (2000).
[5] B. Gutmann, H. Weber, Phase unwrapping with the branch-cut method; role of phase-field direction, Applied Optics 39 (26) (2000) 4802–4816.
[6] B. Gutmann, Investigation of Phase Field for Strip Projection Techniques Using with the Advanced Branch-cut Method, Doctoral thesis, University of Karlsruhe, Shaker Verlag, in German (2000).
[7] T. Wilson, Confocal microscopy, Academic Press Ltd, London, 1990.
[8] C. Kessler-Kramer, V. Mechtcherine, H.S. Müller, Testing and modeling the behavior of concrete under cyclic tensile loading, in: V.C. Li, et al., (Eds.), Fracture Mechanics of Concrete Structures, Ia-FraMCos, 2004, pp. 995–1004.
[9] V. Mechtcherine, H.S. Müller, Fractological investigations on the fracture in concrete, in: R. de Borst, et al., (Eds.), Fracture Mechanics of Concrete Structures, Balkema Publishers, 2001, pp. 81–88.
[10] V. Mechtcherine, H.S. Müller, Analysis of concrete fracture using a heterogeneous continuum model, in: N. Bicanic, et al., (Eds.), Computational Modelling of Concrete Structures (EURO-C 2003), Balkema Publishers, Lisse, The Netherlands, 2003, pp. 81–88.
[11] RILEM TC-122-MLC, State of the art report on micro-cracking and lifetime of concrete — part 1 Prepared by A. D. Jensen and S. Chatterji, Materials and Structures 29 (1996) 3–8.
[12] A. Carpinteri, B. Chiaia, S. Invernizzi, Three-dimensional fractal analysis of microstructural morphologies in concrete, in: H. Mihashi, K. Rokugo (Eds.), Fracture Mechanics of Concrete Structures, Aedificatio Publishers, 1998, pp. 377–386.
[13] P.E. Petersson, Crack growth and development of fracture zones in plain concrete and similar materials, Report TVBM-1006, Division of Building Materials, University of Lund, 1981.
[14] G. Wischers, Zementreihe der Zementindustrie, 1961, p. 173.
[15] P. Gödde, Rechnerische Untersuchungen zur Betonzugfestigkeit unter hoher Belastungsgeschwindigkeit, Universität Dortmund, Dissertation, 1986.
[16] A.J. Zielinski, Fracture of Concrete and Mortar Under Uniaxial Impact Tensile Loading. Doctoral thesis, Delft University of Technology, 1982.